Efficient inverted quantum-dot light-emitting devices with TiO_2/ZnO bilayer as the electron contact layer

Wei Xu,[1,2] Wenyu Ji,[1,*] Pengtao Jing,[1] Xi Yuan,[1,2] Y. A. Wang,[3] Weidong Xiang,[4] and Jialong Zhao[1,5,6]

[1]*State Key Laboratory of Luminescence and Applications, Changchun Institute of Optics, Fine Mechanics and Physics, Chinese Academy of Sciences, Changchun 130033, China*

[2]*University of Chinese Academy of Sciences, Beijing 100039, China*

[3]*Ocean NanoTech, LLC 2143 Worth Lane, Springdale, Arkansas 72764, USA*

[4]*College of Chemistry and Materials Engineering, Wenzhou University, Wenzhou 325035, China*

[5]*College of Mechanical and Electrical Engineering, Wenzhou University, Wenzhou 325035, China*

[6]*e-mail: zhaojl@ciomp.ac.cn*

**Corresponding author: jlu__jwy@163.com*

Received September 19, 2013; revised November 6, 2013; accepted December 15, 2013; posted December 16, 2013 (Doc. ID 197817); published January 20, 2014

We have demonstrated an efficient inverted CdSe/CdS/ZnS core/shell quantum-dot light-emitting device (QD-LED) using a solution-processed sol–gel TiO_2 and ZnO nanoparticle composite layer as an electron-injection layer with controllable morphology and investigated the electroluminescence mechanism. The introduction of the ZnO layer can lead to the formation of spin-coated uniform QD films and fabrication of high-luminance QD-LEDs. The TiO_2 layer improves the balance of charge injection due to its lower electron mobility relative to the ZnO layer. These results offer a practicable platform for the realization of a trade-off between the luminance and efficiency in the inverted QD-LEDs with TiO_2/ZnO composites as the electron contact layer.

OCIS codes: (160.4236) Nanomaterials; (230.3670) Light-emitting diodes; (260.3800) Luminescence; (230.4170) Multilayers.

http://dx.doi.org/10.1364/OL.39.000426

Semiconductor II–VI quantum dots (QDs) have been extensively investigated for potential applications in full-color flat-panel displays or as low-power-consumption solid-state lighting sources because of their unique size-dependent optoelectronic properties, such as narrow emission band [full width at half-maximum (FWHM) ~18–30 nm] and tunable emission in the full visible spectral range, which offer significant advantages for colloidal QD-emitter-based light-emitting devices (QD-LEDs) over liquid crystal displays or organic LEDs [1–5]. Since the first QD-LEDs reported, systematic efforts on nonblinking QDs [6,7], closely packed QD layer deposition [1,2,8] and better device architecture [1,9] have been made to improve the performance of QD-LEDs. To date, the most conventional inorganic/organic hybrid QD-LEDs are composed of a QD layer sandwiched between organic hole and electron transporting layers. However, this classic device structure directly limits the choice of the organic hole injection and transport materials when the orthogonal solvents are used to minimize material intermixing of the bilayers in the sequential spin-coating process of device fabrication. Recently, to overcome this disadvantage, a new inverted QD-LED structure featuring sol–gel TiO_2 or ZnO nanoparticles as the electron-injection layer (EIL) has been designed [9–12]. The inverted QD-LEDs exhibit excellent electroluminescence (EL) properties, such as low turn-on voltage, high maximum brightness, and external quantum efficiency compared to the conventional hybrid devices [9–12]. These improvements are attributed to both TiO_2 and ZnO as inorganic metal-oxide materials with good electron mobility, which facilitate efficient electron injection and transport from the EIL into QDs [9–11]. On the other hand, the inverted device performance can be further optimized by thermal evaporation of kinds of organic materials as hole injection and transport layers with proper energy levels [9,11,12]. Both TiO_2- and ZnO-based inverted QD-LEDs potentially allow for a new possibility to control the morphology and integrity of the QD layer as the only exciton recombination zone, hence achieving high light-emission efficiency. However, the performance of devices based on TiO_2 and ZnO is very different. Rational device structure design for selecting TiO_2 or ZnO is still an open problem. A detailed comparison and investigation on structural and EL properties of TiO_2- and ZnO-based QD-LEDs is highly desirable.

In this study, we fabricated the inverted QD-LEDs with CdSe/CdS/ZnS core/shell QDs as the emitters with emission peak of 624 nm and FWHM of 24 nm. The TiO_2, TiO_2/ZnO, and ZnO were utilized to deeply understand the underlying mechanism of efficient inverted QD-LEDs with different metal-oxide materials as the EIL. The charge injection and balance were investigated through different EILs with controllable morphology. In addition, the rise of current efficiency with increasing current density from 0.1 to 20 mA/cm^2 was attributed to the negatively charged QDs. The QD-LEDs consisted of glass substrates coated with indium-tin-oxide (ITO)/EIL (45 nm)/QDs (~3 mLs)/hole transport layer (50 nm)/MoO_3 (8 nm)/Al (100 nm). The ITO glass substrates were cleaned in an ultrasonic bath with isopropyl alcohol, acetone, and methanol sequentially. ZnO nanoparticles were synthesized by the previously reported method [13]. The TiO_2 (45 nm), TiO_2(20 nm)/ZnO(25 nm), and ZnO (45 nm) were used as EIL for Devices A, B, and C, respectively. A TiO_2 sol–gel precursor (DuPont tyzol BTP) was

diluted (7 wt. % for Device A and 4 wt. % for Device B) in butanol for spin-coating on ITO substrates. ZnO nanoparticles dissolved in butanol with a concentration of 15 mg/mL for Device B and 25 mg/mL for Device C were spin-coated on TiO_2 and ITO films. Spin-coating was performed at 2,000 rpm for 60 s. Then the obtained films were subsequently annealed at 110°C for 30 min in a glove box (MBRAUN) and naturally cooled to room temperature. After that, QDs [with optical density (OD) of ~3.2 at a wavelength of 616 nm, which was estimated from the diluted solution] dissolved in toluene were deposited by spin-coating at 2000 rpm, followed by drying in the glovebox at 70°C for 30 min. Then, 4, 4-N, N-dicarbazole-biphenyl (CBP), MoO_3, and Al were successively deposited by thermal evaporation at a pressure below 4×10^{-6} Torr. The layer thickness and the deposition rate of the materials were monitored *in situ* using an oscillating quartz thickness monitor; the deposition rates of both organic materials and MoO_3 were controlled to be about 0.2 nm/s, and the deposition rates of metal was controlled to be 0.5 nm/s. The characteristics of current-voltage-luminance and EL spectra were measured by a programmable Keithley model 2400 power supply and a Minolta Luminance Meter LS-110, respectively, in air at room temperature. For all devices, no external package or encapsulation was applied after device fabrication.

The CdSe/CdS/ZnS core/shell QDs were synthesized by using the same method in our pervious reports [10,14]. Figure 1 shows the transmission electron microscope (TEM) image (Philips TECNAI G2, inset), photoluminescence (PL), and absorption spectra (Hitachi F-4500 spectrophotometer and UV-3101PC UV-Vis-NIR scanning spectrophotometer [Shimadzu]) of the CdSe/CdS/ZnS core/shell QDs. The average diameter of the QDs is determined to be ~7.5 nm with an emission peak of 624 nm. No defect-related emission below the band edge PL is observed in these QDs, indicating high quality of the QDs. The PL quantum yield was estimated to be ~60% [10]. Figures 2(a)–2(d) show the scanning electron microscope (SEM) (Hitachi S4800) images of the TiO_2, TiO_2/QDs, ZnO, and ZnO/QDs on the ITO substrates, respectively. As can be seen from Fig. 2(a), a homogeneous TiO_2 layer without cracks and interspaces is obtained on ITO substrate, and the detailed topography properties of the TiO_2 film are shown by atomic force microscope

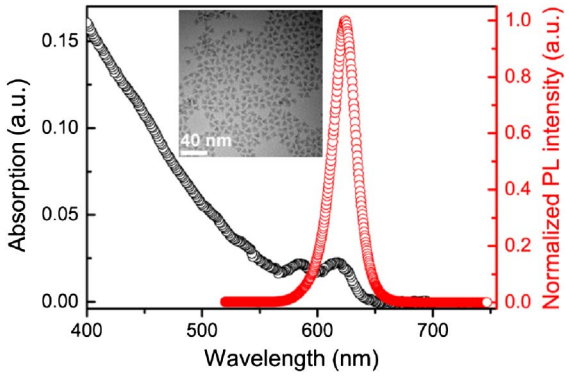

Fig. 1. TEM image (inset), PL (right), and absorption (left) spectra of the CdSe/CdS/ZnS QDs.

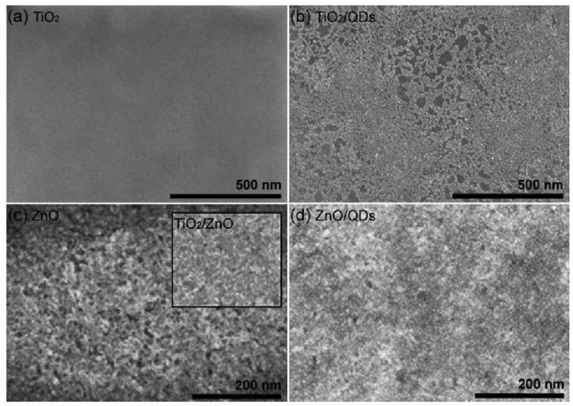

Fig. 2. SEM images of (a) TiO_2, (b) TiO_2/QDs, (c) ZnO, and (d) ZnO/QDs on ITO substrates. The inset in Fig. 2(c) shows an SEM image of TiO_2/ZnO with the same scale bar.

(AFM) (Nanosurf EasyScan2 FlexAFM) images later. When depositing QDs on the TiO_2 layer, organic-soluble QDs tend to aggregate and form closely packed and organized structures as shown in Fig. 2(b). This similar clusterization behavior has previously been demonstrated [15]. In principle, the TiO_2 layer is hydrophilic and the QDs solution in toluene is hydrophobic, as reported previously [10]. As a result, it is not easy to form a high-quality, closely packed QD film on a TiO_2 layer. Figure 2(c) shows the SEM image of ZnO nanoparticles on ITO substrate. Some streaks of imperfections are observed for the ZnO film. But this phenomenon is suppressed partly when depositing ZnO nanoparticles on a TiO_2 layer as shown in the inset of Fig. 2(c). We can see from Fig. 2(d) that a closely packed QD film is obtained, which might originate from the higher surface energy of ZnO nanoparticles. Consequently, a high-quality, closely packed QD film is achieved after ZnO nanoparticles are deposited on the TiO_2 layer.

As shown in Fig. 3(a), the normalized EL spectrum is saturated with QD emission and is slightly redshifted (8–12 nm) from the PL spectra in toluene. We attribute this redshift to a combination of interdot interactions and the electric-field-induced Stark effect [16,17]. It is valuable to note that although the deposited QD film is inconsecutive in the TiO_2-based devices, there is no parasitic emission from adjacent CBP as seen similarly in the other two devices, which indicates that the efficient exciton recombination region only exists inside the QD layer. However, as seen from the voltage–luminance curves of Devices A, B, and C in Fig. 3(b), a higher turn-on voltage (the voltage at the luminance of 1 cd/m^2) of 3.4 V is obtained for the TiO_2-based device relative to the turn-on voltages of 2.4 and 2.5 V for ZnO and TiO_2/ZnO-based devices, respectively. The maximum luminance of the red QD-LEDs is 2119, 2908, and 3861 cd/m^2 for TiO_2, TiO_2/ZnO, and ZnO-based devices, respectively. The increase of 37% and 82% is obtained for TiO_2/ZnO and ZnO-based devices, respectively, compared to the TiO_2-based device. Figure 3(c) shows the voltage–current density characteristics of Devices A, B, and C. As can be seen, the ZnO-containing device possesses higher current density than the TiO_2-based device as the operation voltages increased, which is due to the difference between

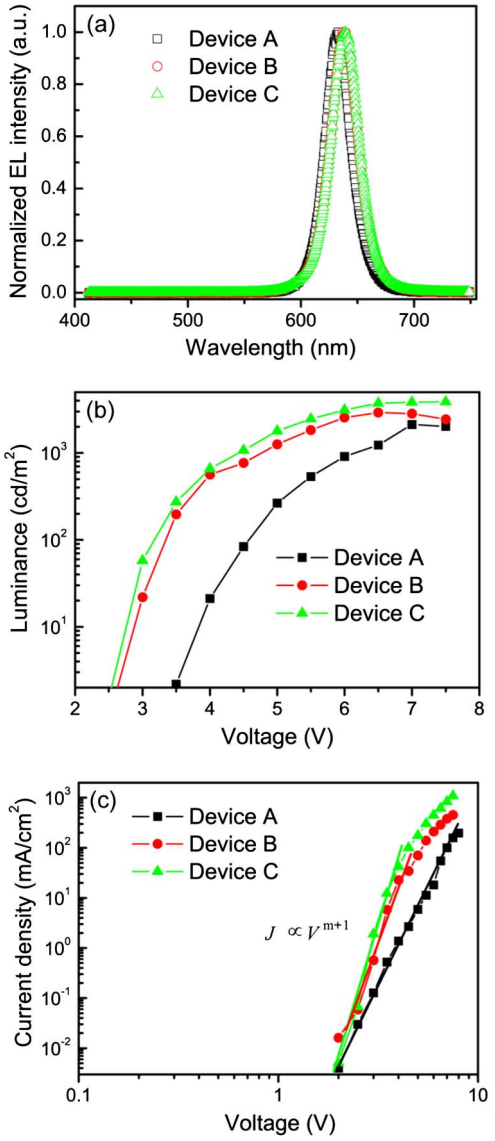

Fig. 3. Normalized EL spectra of Devices A, B, and C at voltage of (a) 6 V, (b) voltage-luminance, and (c) voltage–current density characteristics of Devices A, B, and C.

the electron mobilities of ZnO ($\sim 1.3 \times 10^{-3}$ cm^2 V^{-1} s^{-1}) and TiO_2 ($\sim 1.7 \times 10^{-4}$ cm^2 V^{-1} s^{-1}) [8,9]. Here we further discuss the trap behavior in different EILs through the device current density–voltage characteristics at low operation voltages [11], which exhibit similar space–charge limited conduction behavior with traps as reported in organic LEDs [18]. The J–V characteristics of these devices are well described by the power law of $J \propto V^{m+1}$. The value of m is ~7.3, ~12.4, and ~15.0 for Devices A, B, and C, respectively. The calculated m for the ZnO-based device is much higher than that of TiO_2-based device, which indicates that the electron traps in ZnO film are much more than those of the TiO_2 film. This may be one reason for a lower peak current efficiency in the ZnO-based device than that of TiO_2-based device as seen in Fig. 4.

Figure 4 shows the current density–efficiency characteristics of Devices A, B, and C. For Devices A, B, and C, the peak current efficiency decreases from 5.0 to 3.9 (22%) and 3.0 (40%) due to introduction of the ZnO layer.

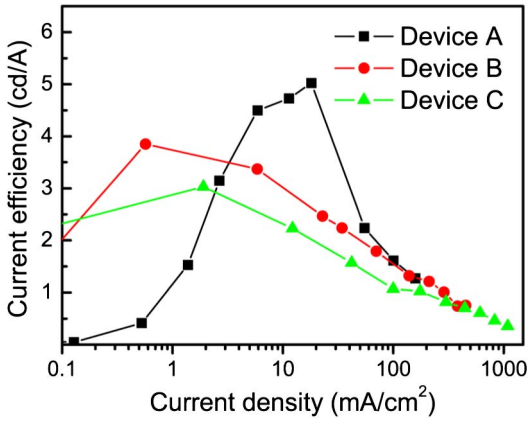

Fig. 4. Current density–efficiency characteristics of Devices A, B, and C.

We ascribe the decrease in device efficiency to the different charge balance. In the ZnO-based device, the electron will be the majority carrier in the QD layer due to the high electron mobility and low electron injection barrier between ZnO and QDs relative to the hole injection barrier between CBP and QDs. As we know, the imbalanced charge injection in the QD layer will lead to the QD charging, quenching the QD luminescence via the nonradiative Auger recombination mechanism, which may be the dominant process limiting the efficiency of QD-LEDs [19–21]. However, in the TiO_2-based device, the amount of electrons in QD layer will decrease owing to the lower electron mobility of the TiO_2 layer. Consequently, a more balanced charge injection in the QD layer can be achieved. These results are also in good agreement with the current density characteristics due to the difference between the electron mobilities of the ZnO and TiO_2 layers. In addition, we further analyzed the voltage–current density–efficiency characteristics at low operation voltages of the three devices to deeply understand the underlying mechanism for different EIL-based devices. We can see that ZnO-containing devices reach their maximum efficiencies at rather low current densities (less than 2 mA/cm^2), but TiO_2-based device reaches the peak efficiency at the higher current density of 20 mA/cm^2 and shows a rise of current efficiency as the current density increases from 0.1 to 20 mA/cm^2. The observed rise in Device A can be explained as part of the QDs in an initial (darkened) negatively charged state due to the electrons injected from TiO_2 and no hole injection owing to the high barrier between CBP and QD for holes. With increasing the current density (voltage), the amount of holes injected into QDs increases, which consequently decreases the probability of QD charging and enhances the device efficiency. In contrast, an Auger assisted energy upconversion hole injection occurring at the CBP/QD interface is proposed due to the high electron mobility of the ZnO nanoparticle layer [11], which leads to an efficient hole injection into the QD layer. As a result, high efficiency is achieved in the ZnO-based device at a lower current density. These results indicate that the TiO_2/ZnO bilayer can not only enhance the quality of the QD film due to the smoother morphology resulting from the synergic effect of small roughnesses as seen in Fig. 5 (AFM images of ITO, ITO/TiO_2,

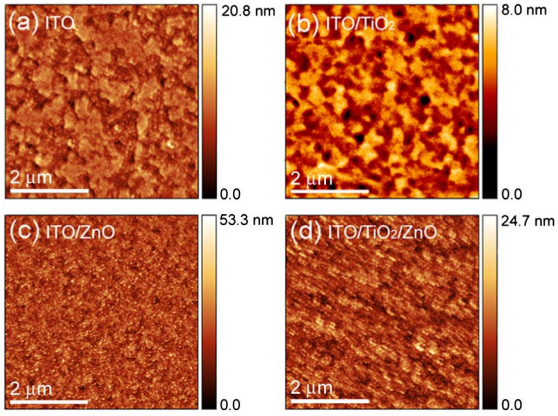

Fig. 5. AFM images of (a) ITO, (b) ITO/TiO_2, (c) ITO/ZnO, and (d) ITO/TiO_2/ZnO; the corresponding root mean square (RMS) roughness is 2.0, 0.98, 5.4, and 2.7 nm, respectively.

ITO/ZnO, and ITO/TiO_2/ZnO, respectively) and higher surface energy of the ZnO nanoparticle layer but can also improve the balance of the injected charge due to the lower electron mobility of TiO_2. The synergic effect of a TiO_2/ZnO composite electron contact layer helps to obtain a trade-off between the luminance and efficiency of QD-LEDs.

In summary, we have fabricated efficient inverted QD-LEDs using TiO_2, ZnO, and TiO_2/ZnO as the electron contacts and colloidal CdSe/CdS/ZnS core/shell QDs as the light emitter. A saturated EL originating from QDs with no emission from organic materials and deep traps in QDs is obtained. A trade-off between the luminance and efficiency of QD-LEDs can be achieved in the inverted QD-LEDs by utilizing a TiO_2/ZnO composite electron contact layer with the controllable morphology. The higher current efficiency for the TiO_2-based device is ascribed to the more balanced charge injection into the QD layer relative to the ZnO-based device. The composite electron contact layer of TiO_2/ZnO combines the advantages of more balanced charge injection of TiO_2 and larger surface energy of the ZnO nanoparticles layer.

This research was supported by the National Natural Science Foundation of China (Nos. 61205025 and 11274304) and the Project Supported by State Key Laboratory of Luminescence and Applications.

References

1. S. Coe, W.-K. A. Woo, M. G. Bawendi, and V. Bulovic, Nature **420**, 800 (2002).
2. E. Matioli, S. Brinkley, K. Kelchner, Y. Hu, S. Nakamura, S. DenBaars, J. Speck, and C. Weisbuch, Light Sci. Appl. **1**, e22 (2012).
3. C. Xiang, W. Koo, F. So, H. Sasabe, and J. Kido, Light Sci. Appl. **2**, e74 (2013).
4. Y. Shirasaki, G. J. Supran, M. G. Bawendi, and V. Bulović, Nat. Photonics **7**, 13 (2013).
5. S. Kim, S. H. Lm, and S.-W. Kim, Nanoscale **5**, 5205 (2013).
6. X. Wang, X. Ren, K. Kahen, M. A. Hahn, M. Rajeswarn, S. Maccagnano-Zacher, J. Silcox, G. E. Cragg, A. L. Efros, and T. D. Krauss, Nature **459**, 686 (2009).
7. Y. Ghosh, B. D. Mangum, J. L. Casson, D. J. Williams, H. Htoon, and J. A. Hollingsworth, J. Am. Chem. Soc. **134**, 9634 (2012).
8. T.-H. Kim, K.-S. Cho, E. K. Lee, S. J. Lee, J. Chae, J. W. Kim, D. H. Kim, J.-Y. Kwon, G. Amaratunga, S. Y. Lee, B. L. Choi, Y. Kuk, J. M. kim, and K. Kim, Nat. Photonics **5**, 176 (2011).
9. J. H. Kwak, W. K. Bae, D. G. Lee, I. Park, J. H. Lim, M. J. Park, H. D. Cho, H. J. Woo, D. Y. Yoon, K. H. Char, S. H. Lee, and C. H. Lee, Nano Lett. **12**, 2362 (2012).
10. W. Y. Ji, P. T. Jing, J. L. Zhao, X. Y. Liu, Y. Q. Wang, and H. B. Li, Nanoscale **5**, 3474 (2013).
11. B. S. Mashford, M. Stevenson, Z. Popovic, C. Hamilton, Z. Zhou, C. Breen, J. Steckel, V. Bulovic, M. G. Bawendi, S. Coe-Sullivan, and P. T. Kazlas, Nat. Photonics **7**, 407 (2013).
12. W. Y. Ji, P. T. Jing, W. Xu, X. Yuan, Y. J. Wang, J. L. Zhao, and A. K.-Y. Jen, Appl. Phys. Lett. **103**, 053106 (2013).
13. C. Pacholski, A. Kornowski, and H. Weller, Angew. Chem. Int. Ed. **41**, 1188 (2002).
14. W. Y. Ji, P. T. Jing, and J. L. Zhao, J. Mater. Chem. C **1**, 470 (2013).
15. S. Chaudhary, M. Ozkan, and W. C. W. Chan, Appl. Phys. Lett. **84**, 2925 (2004).
16. C. R. Kagan, C. B. Murray, and M. G. Bawendi, Phys. Rev. B **54**, 8633 (1996).
17. J.-M. Caruge, J. E. Halpert, V. Bulović, and M. G. Bawendi, Nano Lett. **6**, 2991 (2006).
18. A. J. Campbell, D. D. C. Bradley, and D. G. Lidzey, J. Appl. Phys. **82**, 6326 (1997).
19. J. I. Climente, J. L. Movillla, and J. Planelles, Small **8**, 754 (2012).
20. G. E. Cragg and A. L. Effros, Nano Lett. **10**, 313 (2010).
21. I. Robel, R. Gresback, U. Kortshagen, R. D. Schaller, and V. I. Klimov, Phys. Rev. Lett. **102**, 177404 (2009).